Experimental Validation of Prefabricated Component Manipulation with a Lab-Scale Fully Constrained Cable-Driven Parallel Robot

Yifang Liu[1], Joshua Harrington[2], and Bryan P. Maldonado[1]

***Abstract*— Cable-driven parallel robots (CDPRs) are gaining more attention in the construction field, especially in manipulating and installing large prefabricated components. Our preceding simulation study demonstrated that dynamically feasible, constraint-satisfying trajectories can be generated for a fully constrained six-anchor CDPR performing prefabricated component manipulation. This paper closes the simulation-to-hardware gap by executing trajectories generated with that optimization method on a lab-scale CDPR. A hierarchical pose control architecture is employed to regulate trajectory tracking performance. Experimental results demonstrate that our CDPR achieves terminal position errors below $5\,\mathrm{mm}$ and terminal orientation errors no greater than 1.1° under both nominal conditions and blower-induced aerodynamic disturbances.**

I. Introduction

Prefabricated building components can improve construction productivity and quality, but their installation often requires the controlled manipulation of large elements within confined or access-limited workspaces. Conventional lifting equipment [1] can transport these components efficiently, yet accurate final positioning often depends on substantial manual intervention. Cable-driven parallel robots (CDPRs) offer an alternative approach because their lightweight actuation system, large workspace, and high payload-to-weight ratio are well suited to construction-scale manipulation [2].

Most spatial CDPRs use more cables than the number of controlled degrees of freedom. This actuation redundancy generally enlarges the wrench-feasible workspace and provides greater flexibility in distributing cable tensions, but it also increases the number of actuators, anchors, and supporting structures required for deployment [3]. In particular, installing the two additional actuation and anchoring assemblies at elevated, otherwise unsupported locations may require dedicated structures, such as the roof-mounted cantilever beams used in the European Hephaestus project [4]. A fully constrained six-anchor CDPR eliminates this redundancy and can therefore reduce hardware and installation complexity. Figure 1 illustrates such a system for prefabricated component manipulation. However, the nonredundant configuration also narrows the wrench-feasible workspace, reduces cable-tension margins, and limits the controller's ability to redistribute tension. Consequently, trajectory generation and accurate physical execution become more challenging.

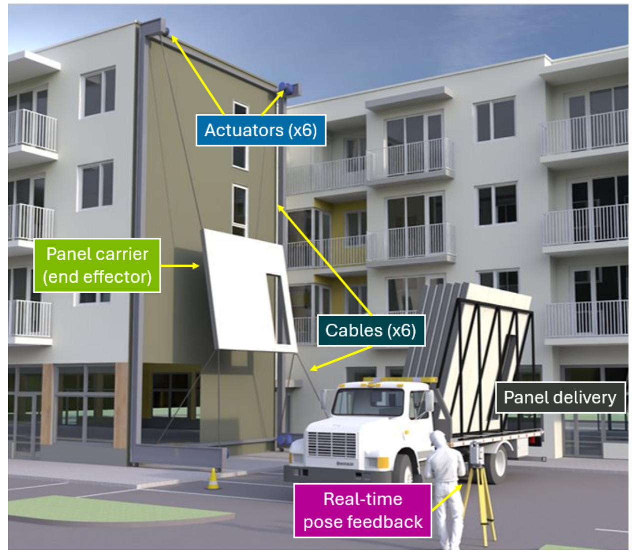

Fig. 1. Conceptual illustration of a fully constrained CDPR for prefabricated facade installation.

Our previous work addressed the planning aspect of this problem by formulating a nonlinear trajectory-optimization method that enforces the CDPR dynamics, cable-tension bounds, and motion constraints [3]. Simulation studies demonstrated that the method can generate dynamically feasible trajectories for idealized, prototype-based, and building-scale six-anchor systems. Nevertheless, simulation feasibility alone does not establish that the planned motion can be executed accurately on physical hardware. Model mismatch, sensor noise, communication delay, and unmodeled actuator and cable behavior can accumulate during execution, while torque regulation without direct pose feedback may be insufficient to achieve the millimeter-scale accuracy required for component placement.

This study addresses the resulting planning-to-execution gap through experimental validation on a lab-scale, fully constrained CDPR. Trajectories and nominal cable tensions are generated using the previously developed optimization

Yifang Liu and Bryan Maldonado are with the Buildings and Transportation Science Division, Oak Ridge National Laboratory, Oak Ridge, TN 37830 USA (e-mail: liuy5@ornl.gov; maldonadopbp@ornl.gov).

[2]Joshua Harrington is with Bredesen Center, The University of Tennessee, Knoxville, TN, USA, e-mail: jharr303@vols.utk.edu

Notice: This manuscript has been authored by UT-Battelle, LLC, under contract DE-AC05-00OR22725 with the US Department of Energy (DOE). The US government retains and the publisher, by accepting the article for publication, acknowledges that the US government retains a nonexclusive, paid-up, irrevocable, worldwide license to publish or reproduce the published form of this manuscript, or allow others to do so, for US government purposes. DOE will provide public access to these results of federally sponsored research in accordance with the DOE Public Access Plan (https://www.energy.gov/doe-public-access-plan). The views expressed herein do not necessarily represent the views of the U.S. Department of Energy or the United States Government.

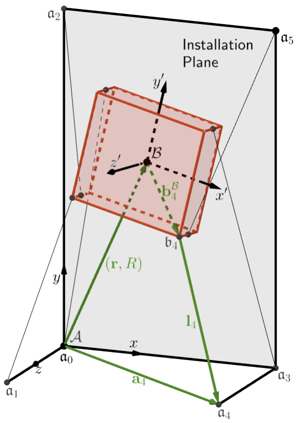

Fig. 2. Geometric definitions for the CDPR physics-based dynamic model.

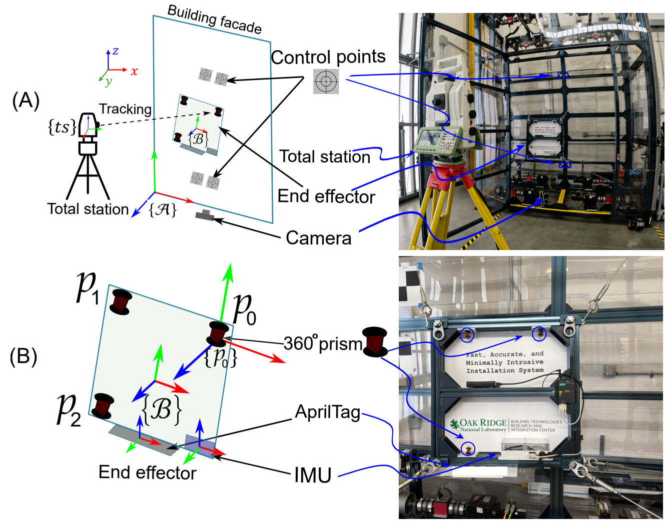

Fig. 3. Lab-scale CDPR and sensing system. Left: conceptual representation of the end effector, sensors, and coordinate frames. Right: physical prototype, showing (A) the complete system and (B) the end effector instrumented with an IMU, three prisms, and an AprilTag.

framework and executed using a hierarchical controller. At the high level, a linear quadratic Gaussian (LQG) controller uses fused pose measurements from a total station, an inertial measurement unit, and an AprilTag-based vision system to compute corrective cable tensions. Mid-level PI loops regulate actuator torque, and a low-level motion controller tracks the resulting motor-position commands.

The system is evaluated under nominal laboratory conditions and under aerodynamic disturbances generated using a blower. In the reported tests, the terminal position errors were below $5\,\mathrm{mm}$, and the terminal orientation errors were below $1.1°$. These results provide initial physical evidence that optimized trajectories for a reduced-anchor CDPR can be executed with millimeter-scale terminal positioning accuracy while maintaining approximately degree-level orientation accuracy.

II. Lab-Scale CDPR System

Figure 2 illustrates the geometry of the fully constrained CDPR. The fixed global frame is denoted by $\{\mathcal{A}\}$, while the body-fixed frame $\{\mathcal{B}\}$ is attached to the moving end effector, shown in red. The end effector is connected to the frame by $n = 6$ massless cables. Cables are guided through swivel pulleys and wound onto drums. For each cable $i \in \{1, \ldots, n\}$, we define the following quantities:

- The constant vectors $\mathbf{a}_i$ denote the proximal anchor points $\mathfrak{a}_i$ in the frame with respect to $\{\mathcal{A}\}$.
- The constant vectors $\mathbf{b}_i^{\mathcal{B}}$ denote the distal anchor points $\mathfrak{b}_i$ in the end effector with respect to $\{\mathcal{B}\}$.
- The pose $(\boldsymbol{r}, R)$ consists of the end effector's center of mass position $\boldsymbol{r} = \begin{bmatrix} r_x & r_y & r_z \end{bmatrix}^T$ in $\{\mathcal{A}\}$ and the rotation matrix $R \in SO(3)$ that maps $\{\mathcal{B}\}$ to $\{\mathcal{A}\}$. The corresponding Euler angles are denoted by φ, θ, and ψ.

The experimental platform is adapted from the eight-cable prototype presented in our previous work [5]. For the present study, two cables were disconnected and selected distal attachment points were relocated, yielding the fully constrained six-anchor configuration shown in Figs. 2 and 3.

The robot comprises a rigid aluminum frame measuring $2.7\,\mathrm{m} \times 3.5\,\mathrm{m} \times 1.5\,\mathrm{m}$ (width $\times$ height $\times$ depth) and an end effector measuring $0.63\,\mathrm{m} \times 0.68\,\mathrm{m} \times 0.13\,\mathrm{m}$, and the mass of the end effector is $22.89\,\mathrm{kg}$. Six cables connect proximal attachment points on the frame to corresponding distal attachment points on the end effector. Each cable is driven by a servomotor coupled to a high-ratio gearbox, providing accurate encoder-based position control and resistance to backdriving. Each actuator assembly also includes a torque sensor for feedback control, a constant-radius spiral drum for cable winding, and a pulley that guides the cable toward its distal attachment point. The drum radius is $\rho = 0.0691\,\mathrm{m}$ and is used to estimate cable tension from the measured actuator torque.

During prefabricated component manipulation, the end effector serves as the component carrier and must be accurately guided from a pickup pose to a designated placement pose. Closed-loop execution therefore requires real-time estimates of both its position and orientation. As illustrated in Fig. 3, the prototype combines three complementary sensing modalities: (i) a construction-grade total station for high-accuracy static pose measurements and dynamic position tracking; (ii) an inertial measurement unit (IMU) with an onboard attitude and heading reference system (AHRS) for real-time orientation estimation; and (iii) a camera-based AprilTag detector that provides periodic yaw corrections.

Three $360°$ prisms, denoted by p_0, p_1, and p_2, are mounted on the end effector. Let $\boldsymbol{p}_i^{\mathcal{A}}$ denote the position of prism p_i expressed in the global robot frame $\{\mathcal{A}\}$. Unless otherwise stated, all position vectors are expressed in $\{\mathcal{A}\}$, and the superscript is omitted for brevity. Superscripts are retained when quantities are expressed in other coordinate frames.

The prisms are arranged such that $\boldsymbol{p}_0 - \boldsymbol{p}_1$, directed from p_1 to p_0, is aligned with the x-axis of the end-effector body frame $\{\mathcal{B}\}$, whereas $\boldsymbol{p}_1 - \boldsymbol{p}_2$ is aligned with its y-axis. The body frame $\{\mathcal{B}\}$ and the prism frame $\{p_0\}$ have the same orientation and differ only by a fixed translation. The origin

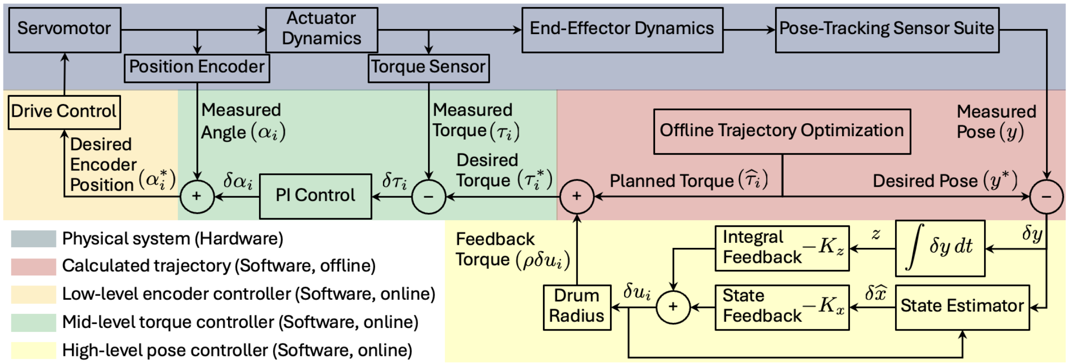

Fig. 4. Hierarchical control architecture implemented on the lab-scale CDPR.

of $\{\mathcal{B}\}$ is located at the end-effector centroid, while the origin of $\{p_0\}$ is located at prism p_0. Given the prism configuration, the centroid of the end effector is defined as the midpoint between prisms p_0 and p_2, calculated as $\boldsymbol{r} = 1/2(\boldsymbol{p}_0 + \boldsymbol{p}_2)$.

III. Control Architecture

To achieve precise CDPR control ensuring safe and reliable operation, we adopt a hierarchical control architecture consisting of three levels: low-level drive control, mid-level torque control, and high-level pose control. The low-level controller directly regulates the servomotors and is essential for interfacing with the hardware. Sitting above it, the torque controller ensures safe operation by maintaining appropriate cable tensions, thereby preventing slack or breakage during motion. Torque control is effective in bringing the end-effector close to the desired pose, with position errors on the order of centimeters to decimeters. However, due to uncertainties in system modeling and the lack of direct pose feedback, torque control alone cannot achieve millimeter-level accuracy [6]. To address this limitation, a high-level pose controller was developed and integrated into the control architecture, incorporating real-time end-effector pose feedback into the control loop. The hierarchical control architecture is illustrated in Fig. 4.

Low-level drive control was handled by a Trio P662 eight-axis motion controller, which executes encoder position commands α_i^* for individual servomotors using its embedded real-time encoder position measurements α_i. Mid-level torque control was implemented using an incremental proportional-integral (PI) feedback law on each actuator:

$$\delta\alpha_i = K_P\delta\tau_i + K_I \int \delta\tau_i \, dt. \quad (1)$$

Here, K_P and K_I denote the proportional and integral gains, respectively, and $\delta\tau_i = \tau_i - \tau_i^*$ is the torque error, defined as the difference between the measured torque τ_i and the desired torque τ_i^* for the corresponding actuator. Therefore, the desired encoder position is calculated as $\alpha_i^* = \alpha_i + \delta\alpha_i$ and forwarded to the low-level drive controller. Torque limits are enforced at this stage to prevent both negative torque values and excessively high torque commands. Finally, the high-level controller adopts the LQG framework because

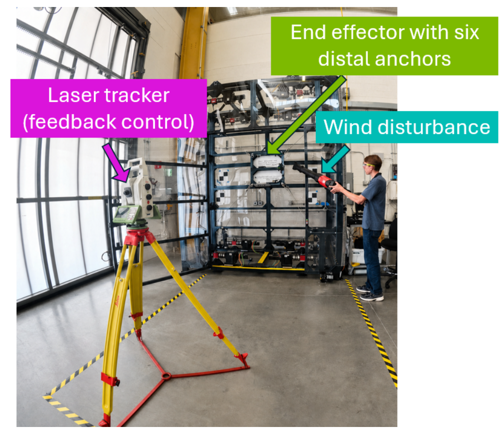

Fig. 5. Experimental setup for the lab-scale CDPR, including the blower used to introduce aerodynamic disturbances.

it offers an optimal balance between multivariate control performance and robustness against model uncertainties and external disturbances [7]. The LQG uses the measured pose y from the integrated sensor suite and the desired pose y^* from the trajectory optimization algorithm to calculate the pose error $\delta y = y - y^*$. Then, it generates corrective cable tension commands δu_i to compensate for pose errors in real time. Thus, the desired torque is $\tau_i^* = \widehat{\tau}_i + \rho\delta u_i$ and forwarded to the mid-level torque controller, where $\widehat{\tau}_i$ is the planned torque estimated from the trajectory optimization.

IV. Experimental Results

The reference trajectory were generated using the constrained trajectory optimization method presented in our previous work [3]. The optimized trajectory was evaluated experimentally under two conditions: nominal trajectory tracking without an applied disturbance and trajectory tracking under blower-induced aerodynamic disturbances. The hierarchical controller described in Section III was used in both cases.

Figure 5 shows the disturbance test configuration. The blower outlet was positioned approximately $0.5\,\mathrm{m}$ to $1.0\,\mathrm{m}$ from the end effector and directed toward its inner surface. As shown in the bottom plot of Fig. 6, the blower

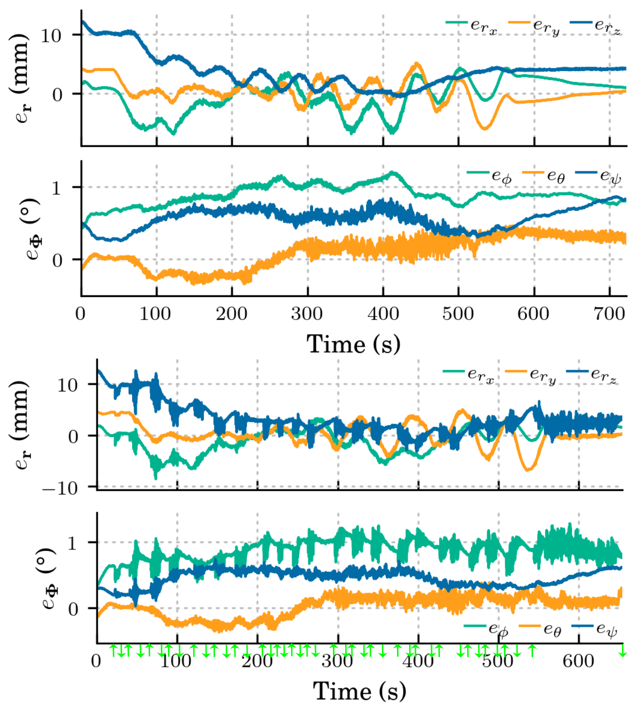

Fig. 6. End effector trajectory tracking errors under nominal conditions (top) and blower-induced aerodynamic disturbances (bottom). Upward arrows indicate wind disturbance ON, and downward arrows indicate wind disturbance OFF.

was activated intermittently during trajectory tracking for randomized intervals of 5 s to 20 s. After the end effector reached steady state, the blower operated continuously for the remainder of the experiment. The blower outlet was also swept laterally and vertically to vary the direction of the applied aerodynamic load. This procedure was intended to introduce time-varying disturbances.

Figure 6 compares the position and orientation tracking errors for the two test conditions. The initial position error is greater than 10 mm. After this, the component-wise position errors oscillated but remained below 10 mm during trajectory execution. The three orientation-error components remained below 1.5° in both tests, indicating that the controller maintained comparable tracking performance in the presence of the imposed disturbances. Both the hierarchical controller and the data acquisition system operated at 25 Hz; thus, the evaluation window corresponds to the final 40 s of each test. The position error is defined as the Euclidean distance between the measured and reference positions, while the orientation error is calculated as the Riemannian (geodesic) distance between the measured and reference rotations in $SO(3)$. The mean position errors were 4.3 mm under nominal conditions and 3.1 mm under aerodynamic disturbances. The corresponding mean orientation errors were 1.1° and 1.0°, respectively. Although the mean errors were comparable, the blower disturbance test exhibited larger standard deviations in both position and orientation, indicating greater variability under the imposed aerodynamic loading.

TABLE I

POSE ERROR STATISTICS OVER THE FINAL 1000 SAMPLES UNDER HIERARCHICAL CONTROL.

	Position error (mm)		Orientation error (°)	
Test condition	Mean	Std. dev.	Mean	Std. dev.
Nominal	4.3	0.056	1.1	0.013
Blower disturbance	3.1	0.60	1.0	0.062

V. Conclusions

This paper experimentally validated optimized trajectory execution on a lab-scale, fully constrained CDPR for prefabricated component manipulation. The proposed control architecture includes a high-level LQG pose feedback, mid-level PI torque regulation, and low-level motor-position control. Experiments conducted under nominal conditions and blower-induced aerodynamic disturbances demonstrated bounded trajectory tracking errors. These results provide initial physical evidence that a fully constrained CDPR can execute dynamically feasible trajectories with millimeter-scale terminal positioning accuracy under laboratory conditions. Future work will evaluate repeatability over a larger number of trials and manipulation tasks, refine the hierarchical controller and estimator tuning, and extend validation to heavier components and full-scale deployment conditions.

Acknowledgment

This research was supported by the DOE Office of Critical Minerals and Energy Innovation (CMEI), Building Technologies Office, under the guidance of Sven Mumme, and used resources at the Building Technologies Research and Integration Center (BTRIC), a DOE User Facility at Oak Ridge National Laboratory. Research sponsored by the Laboratory Directed Research and Development Program of Oak Ridge National Laboratory, managed by UT-Battelle, LLC, for the U. S. Department of Energy.

References

[1] C. Mascheck, "Serielles sanieren: So funktioniert der "energiesprong"," accessed: 2026-08-23. [Online]. Available: https://cradle-mag.de/artikel/serielles-sanieren-energiesprong.html

[2] R. Hu, K. Iturralde, T. Linner, C. Zhao, W. Pan, A. Pracucci, and T. Bock, "A simple framework for the cost–benefit analysis of single-task construction robots based on a case study of a cable-driven facade installation robot," *Buildings*, vol. 11, no. 1, 2021.

[3] Y. Liu, N. W. Hayes, D. Hun, and B. P. Maldonado, "Dynamic analysis of fully constrained cable-driven parallel robots for automated prefabricated component installation," *Automation in Construction*, vol. 190, p. 107062, 2026.

[4] K. Iturralde, M. Feucht, D. Illner, R. Hu, W. Pan, T. Linner, T. Bock, I. Eskudero, M. Rodriguez, J. Gorrotxategi *et al.*, "Cable-driven parallel robot for curtain wall module installation," *Automation in Construction*, vol. 138, p. 104235, 2022.

[5] Y. Liu, N. W. Hayes, B. Selvakumar, D. Hun, and B. P. Maldonado, "Lab-scale cable-driven parallel robot prototype for automated prefabricated component manipulation," *Journal of Computing in Civil Engineering*, vol. 40, no. 5, p. 04026066, 2026.

[6] Y. Hu, L. Tao, J. Jia, and W. Lv, "Control and simulation of cable-driven parallel robots in offshore cargo handling," in *Proceeding of the 11th World Congress on Intelligent Control and Automation*, 2014, pp. 2451–2455.

[7] G. Chen, S. Hutchinson, and F. Dellaert, "Locally optimal estimation and control of cable driven parallel robots using time varying linear quadratic gaussian control," in *2022 IEEE/RSJ International Conference on Intelligent Robots and Systems (IROS)*, 2022, pp. 7367–7374.